2001

Modeling of a Nickel-Hydrogen Cell: Phase Reactions in the Nickel Active Material

B. Wu

Ralph E. White
University of South Carolina - Columbia, white@cec.sc.edu

Publication Info

Published in *Journal of the Electrochemical Society*, Volume 148, Issue 6, 2001, pages A595-A609.

Wu, B., & White, R.E. (2001). Modeling of a Nickel-Hydrogen Cell. Phase Reactions in Nickel Active Material. *Journal of the Electrochemical Society*, *148*(6): A595-A609.
Publisher's Version: http://dx.doi.org/10.1149/1.1371799

Journal of The Electrochemical Society, **148** (6) A595-A609 (2001)
0013-4651/2001/148(6)/A595/15/$7.00 © The Electrochemical Society, Inc.

Modeling of a Nickel-Hydrogen Cell

Phase Reactions in the Nickel Active Material

B. Wu and R. E. White[*, z]

Center for Electrochemical Engineering, Department of Chemical Engineering, University of South Carolina, Columbia, South Carolina 29208, USA

A nonisothermal model of a nickel-hydrogen cell has been developed with the consideration of multiple phases in the nickel active material. Important mechanisms inside a nickel-hydrogen cell, such as mass balances of active species, kinetics of electrochemical reactions, and the energy balance of the whole cell, etc., have been included in the model. The model predictions under different conditions are presented and analyzed. These predictions showed that nickel phase reactions have significant influences on the behavior of a nickel-hydrogen cell. Some observed phenomena of a nickel-hydrogen cell, *e.g.*, the capacity variation at different temperatures and the KOH concentration change between charge and discharge processes, could be reflected reasonably with the model.
 [DOI: 10.1149/1.1371799]

Manuscript submitted July 6, 2000; revised manuscript received February 18, 2001.

The nickel-hydrogen battery has been the primary energy storage device in aerospace applications for more than two decades. Compared to the newly developed high-energy-density batteries, *e.g.*, the nickel-metal hydride battery and the lithium-ion battery, the nickel-hydrogen battery still holds the advantages of extraordinarily long cycle life and excellent operating safety (two critical requirements for aerospace energy storage systems), and thus will remain competitive in aerospace applications in the future. A typical nickel-hydrogen cell consists of many cell modules contained in a cylindrical pressure vessel (see Fig. 1). Each cell module has four major components: the nickel positive electrode, the Zircar separator, the platimum negative electrode, and the polypropylene gas screen.[1]

The nickel electrode in a nickel-hydrogen cell is produced by electrochemically impregnating the nickel active material into a sintered nickel substrate. Some cobalt hydroxide is usually added to the nickel active material to improve the cycle life and the charge acceptance of the nickel electrode. The loading of the nickel active material in a nickel-hydrogen cell is lower than that of other nickel-based batteries, in order to improve the cycle life of the nickel electrode. The platinum electrode in a nickel-hydrogen cell is a thin layer of platinum black, Teflon bonded on a nickel screen. It is similar to the electrodes used in the fuel cell. The platinum electrode is half wetted with the KOH electrolyte and provides a good interface for hydrogen and oxygen reactions. Unlike the negative electrodes in other nickel-based batteries, the platinum electrode has no significant deterioration processes. Thus, the life-limiting electrode in a nickel-hydrogen cell turns out to be the nickel electrode. This makes possible the long cycle life of the nickel-hydrogen cell. The electrolyte used in a nickel-hydrogen cell is concentrated KOH solution, which has good electric conductivity for a wide range of temperatures. The concentration of KOH electrolyte has significant influences on the performance of a nickel-hydrogen cell. A high KOH concentration yields a high capacity but a short cycle life while a low KOH concentration leads to a long cycle life but a low capacity. At the activation stage of a nickel-hydrogen cell, some electrolyte is forced out of the cell stack by the gas evolution and is then drained out of the cell. Thus, inside the cell stack there exists some gas volume, which provides good diffusion paths for hydrogen and oxygen gases in normal cell operations.[1]

Some modeling efforts have been made for the nickel-hydrogen battery in the past. Mao *et al.*[2] developed a discharge model of a nickel-hydrogen cell by considering only the main reactions on the electrodes. A pseudo-two-dimensional model of the nickel electrode was utilized to investigate the proton diffusion process in the nickel active material. Their model predicted that proton diffusion could be a limiting factor at high discharge rates. De Vidts *et al.*[3] constructed a comprehensive nickel-hydrogen cell model, which included five reactions and processes in both gas and liquid phases. The predictions of their model showed good agreement with the data obtained from an experimental cell module. Kim *et al.*[4] presented a thermal model of a common-vessel multicell nickel-hydrogen battery. In their model, the temperature distribution inside the battery was calculated with some assumed heat generation rates. Significant temperature gradients near the surface of the nickel-hydrogen battery were predicted from their model. A thermal model with the theoretical heat generation rate was developed later by Kim *et al.*[5] Their model was used to investigate the influence of the location of heat generation on the temperature profile inside the nickel-hydrogen battery, which was found to be insignificant. The model by De Vidts *et al.*[3] was further improved with a general energy balance, temperature dependent parameters, and simplified equations of mass balances.[6] This model predicted that adiabatic operations of a nickel-hydrogen cell were unsafe for both charge and discharge processes. Timmerman *et al.*[7] developed a nickel-hydrogen cell model with simple nickel phase reactions. The predictions of their model showed good qualitative agreement with experimental data of the nickel-hydrogen battery at different temperatures. The proton diffusion process in the nickel active material has been included in some nickel-hydrogen cell models.[2,3,6,7] However, as shown by Paxton and Newman[8] and Motupally *et al.*,[9] proton diffusion is very unlikely to be a limiting factor for a nickel electrode at low charge/discharge rates, and thus it is neglected in this work. The primary objective of this work is to enhance the models by De Vidts *et al.*[6] and Timmerman *et al.*[7] with a comprehensive scheme of phase re-

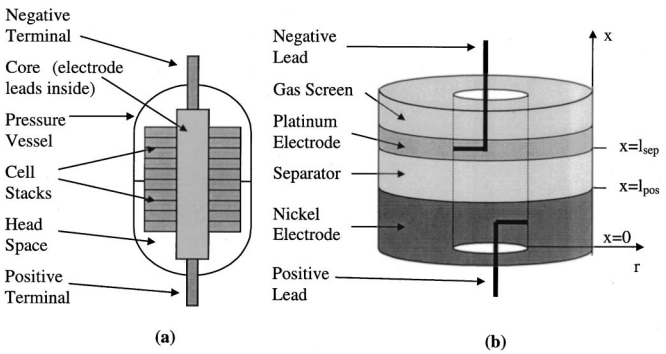

Figure 1. Schematic diagrams of (a) a nickel-hydrogen cell and (b) one module of the cell stack.

* Electrochemical Society Fellow.
z E-mail: white@engr.sc.edu

actions in the nickel active material, and to investigate with the model the effects of nickel phase reactions on the behavior of a nickel-hydrogen cell.

Modeling of a Nickel-Hydrogen Cell

The nickel electrode has been actively researched for a long time. The electrochemical behavior of the nickel active material is usually described by the one-electron-transfer redox reaction between nickel hydroxide and nickel oxyhydroxide. However, experimental data have shown that higher capacities could be obtained from the nickel active material than that expected from the one-electron-transfer reaction, especially at low temperatures and high KOH concentrations. Many schemes of nickel phases have been proposed for the nickel active material in the past.[10-18] The oxidized nickel active material usually exhibits a valence above 3.0. This has been attributed to the existence of two forms of nickel oxyhydroxide: β-NiOOH with a nickel valance of +3 and γ-NiOOH with a nickel valence between +3.5 and +3.8. The β-NiOOH phase has a crystalline structure while the γ-NiOOH phase has an irregular structure with intercalated water molecules and some cations. For the fully reduced nickel active material, there are two forms of nickel hydroxide with a nickel valence of +2: α-$Ni(OH)_2$ and β-$Ni(OH)_2$. The α-$Ni(OH)_2$ phase has an amorphous structure with embedded water molecules while the β-$Ni(OH)_2$ phase has an anhydrous and highly crystalline structure. Many other nickel phases have also been proposed in the literature, but they have not been generally accepted. The reaction scheme among four nickel phases proposed by Bode *et al.*[10] (see Fig. 2) has been widely utilized to describe the behavior of the nickel active material. It was also used in this work. There are two redox paths in the nickel active material: β-$Ni(OH)_2$/β-NiOOH with one electron transfer and α-$Ni(OH)_2$/γ-NiOOH with 1.5-1.8 electrons transfer. The connections between these two paths are the electrochemical conversion of β-NiOOH to γ-NiOOH during overcharge, and the automatic dehydration of α-$Ni(OH)_2$ to β-$Ni(OH)_2$.

The five reactions that have been generally used for a nickel-hydrogen cell are

On the nickel electrode

$$NiOOH + H_2O + e^- \underset{\text{charge}}{\overset{\text{discharge}}{\rightleftarrows}} Ni(OH)_2 + OH^- \quad [1a]$$

$$\beta\text{-}NiOOH \underset{\text{charge}}{\overset{\text{discharge}}{\rightleftarrows}} \beta\text{-}Ni(OH)_2 \quad [1b]$$

$$\frac{1}{2} O_2 + H_2O + 2e^- \rightleftarrows 2OH^- \quad [2]$$

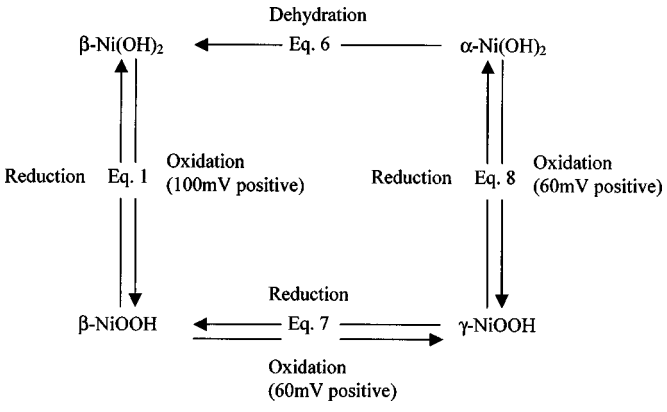

Figure 2. The reaction scheme among nickel phases.

$$\frac{1}{2} H_2 + OH^- \rightarrow H_2O + e^- \quad [3]$$

On the platinum electrode

$$\frac{1}{2} H_2 + OH^- \underset{\text{charge}}{\overset{\text{discharge}}{\rightleftarrows}} H_2O + e^- \quad [4]$$

$$\frac{1}{2} O_2 + H_2O + 2e^- \rightarrow 2\ OH^- \quad [5]$$

Equation 1 is the main reaction on the nickel electrode. Equation 1b is written in explicit nickel phases. Equations 2 and 3 are the side reactions on the nickel electrode. Equation 4 is the main reaction on the platinum electrode. Equation 5 is the side reaction on the platinum electrode. In addition to the above five reactions, three additional nickel phase reactions are also included in this work, as given below

$$\left[Ni(OH)_2 \cdot \frac{2}{3} H_2O\right] \rightarrow Ni(OH)_2 + \frac{2}{3} H_2O \quad [6a]$$

$$\alpha\text{-}Ni(OH)_2 \rightarrow \beta\text{-}Ni(OH)_2 \quad [6b]$$

$$\left[K_{1/3}NiO_2 \cdot \frac{2}{3} H_2O\right] + \frac{1}{3} H_2O + \frac{2}{3} e^- \underset{\text{charge}}{\overset{\text{discharge}}{\rightleftarrows}} NiOOH + \frac{1}{3} K^+ + OH^- \quad [7a]$$

$$\gamma\text{-}NiOOH \underset{\text{charge}}{\overset{\text{discharge}}{\rightleftarrows}} \beta\text{-}NiOOH \quad [7b]$$

$$\left[K_{1/3}NiO_2 \cdot \frac{2}{3} H_2O\right] + 2H_2O + \frac{5}{3} e^- \underset{\text{charge}}{\overset{\text{discharge}}{\rightleftarrows}} \left[Ni(OH)_2 \cdot \frac{2}{3} H_2O\right] + \frac{1}{3} K^+ + 2\ OH^- \quad [8a]$$

$$\gamma\text{-}NiOOH \underset{\text{charge}}{\overset{\text{discharge}}{\rightleftarrows}} \alpha\text{-}Ni(OH)_2 \quad [8b]$$

Equation 6 is a unidirectional chemical reaction that happens through the dissolution of α-$Ni(OH)_2$ and then the crystallization of β-$Ni(OH)_2$. The conversion between β-NiOOH and γ-NiOOH is usually regarded as unidirectional due to the significant structural change accompanying the reverse reaction. However, there is no solid experimental and theoretical basis to support this assertion, because the forward reaction also involves a drastic structure change. In this work, the conversion between β-NiOOH and γ-NiOOH is treated as a reversible electrochemical reaction. In the above reaction equations, the molecular formulas of the β-$Ni(OH)_2$ and β-NiOOH phases are expressed by $Ni(OH)_2$ and NiOOH, respectively, based on their highly crystalline structure. However, there is no consensus on the molecular formulas of the α-$Ni(OH)_2$ and γ-NiOOH phases. The molecular formulas for the α-$Ni(OH)_2$ and γ-NiOOH phases in the above reaction equations are estimated from those in the literature.[10-18] The state of charge (SOC) of a nickel-hydrogen cell used in this work is based on the one-electron-transfer reaction in Eq. 1. It could be larger than one due to the appearance of the γ-NiOOH phase

$$SOC = \frac{c_\beta + 1.67 c_\gamma}{c_{H^+,max}} \quad [9]$$

For the kinetics of the electrochemical reactions Eq. 1-4, 7, and 8, applying the Butler-Volmer equation gives

$$j_1 = i_{o,1,ref,T}\left[\left(\frac{c_e}{c_{e,ref}}\right)\left(\frac{c_{\beta_-}}{c_{\beta_-,ref}}\right)\exp\left(\frac{\alpha_{a,1}F}{RT}\eta_1\right) - \left(\frac{c_{\beta_+}}{c_{\beta_+,ref}}\right)\exp\left(-\frac{\alpha_{c,1}F}{RT}\eta_1\right)\right] \quad [10]$$

$$j_2 = i_{o,2,ref,T}\left[\left(\frac{c_e}{c_{e,ref}}\right)^2\exp\left(\frac{\alpha_{a,2}F}{RT}\eta_2\right) - \left(\frac{c_{O_2}}{c_{O_2,ref}}\right)^{1/2} \times \exp\left(-\frac{\alpha_{c,2}F}{RT}\eta_2\right)\right] \quad [11]$$

$$j_3 = i_{o,3,ref,T}\left[\left(\frac{c_e}{c_{e,ref}}\right)\left(\frac{c_{H_2}}{c_{H_2,ref}}\right)^{1/2}\exp\left(\frac{\alpha_{a,3}F}{RT}\eta_3\right) - \exp\left(-\frac{\alpha_{c,3}F}{RT}\eta_3\right)\right] \quad [12]$$

$$j_4 = i_{o,4,ref,T}\left[\left(\frac{c_e}{c_{e,ref}}\right)\left(\frac{c_{H_2}}{c_{H_2,ref}}\right)^{1/2}\exp\left(\frac{\alpha_{a,4}F}{RT}\eta_4\right) - \exp\left(-\frac{\alpha_{c,4}F}{RT}\eta_4\right)\right] \quad [13]$$

$$j_7 = i_{o,7,ref,T}\left[\left(\frac{c_e}{c_{e,ref}}\right)^{4/3}\left(\frac{c_{\beta_+}}{c_{\beta_+,ref}}\right)\exp\left(\frac{\alpha_{a,7}F}{RT}\eta_7\right) - \left(\frac{c_\gamma}{c_{\gamma,ref}}\right)\exp\left(-\frac{\alpha_{c,7}F}{RT}\eta_7\right)\right] \quad [14]$$

$$j_8 = i_{o,8,ref,T}\left[\left(\frac{c_e}{c_{e,ref}}\right)^{7/3}\left(\frac{c_\alpha}{c_{\alpha,ref}}\right)\exp\left(\frac{\alpha_{a,8}F}{RT}\eta_8\right) - \left(\frac{c_\gamma}{c_{\gamma,ref}}\right)\exp\left(-\frac{\alpha_{c,8}F}{RT}\eta_8\right)\right] \quad [15]$$

The exchange current density of each electrochemical reaction is temperature dependent as described with the Arrhenius equation

$$i_{o,k,ref,T} = i_{o,k,ref,T_0}\exp\left[-\frac{\Delta E_{a,k}}{R}\left(\frac{1}{T} - \frac{1}{T_0}\right)\right] \quad [16]$$

The overpotential for each electrochemical reaction is defined as

$$\eta_k = \phi_{pos} - \phi_1 - \phi_{eq,k,ref,T} \quad \text{at the nickel electrode} \quad [17]$$

$$\eta_k = \phi_{neg} - \phi_1 - \phi_{eq,k,ref,T} \quad \text{at the platinum electrode} \quad [18]$$

The value of $\phi_{eq,k,ref,T}$ with respect to the Hg/HgO reference electrode for each electrochemical reaction is given by the following equations at the reference reactant concentrations

$$\phi_{eq,1,T} = (U_1^\theta - U_{RE}^\theta) + (T - T_0)\left(\frac{dU_1^\theta}{dT} - \frac{dU_{RE}^\theta}{dT}\right) + \frac{RT}{F}\ln\left(\frac{c_{\beta_+}}{c_{\beta_-}}\right) \quad [19]$$

$$\phi_{eq,2,T} = (U_2^\theta - U_{RE}^\theta) + (T - T_0)\left(\frac{dU_2^\theta}{dT} - \frac{dU_{RE}^\theta}{dT}\right) + \frac{RT}{2F}\ln(c_{O_2})^2 \quad [20]$$

$$\phi_{eq,3,T} = (U_3^\theta - U_{RE}^\theta) + (T - T_0)\left(\frac{dU_3^\theta}{dT} - \frac{dU_{RE}}{dT}\right) - \frac{RT}{F}\ln(c_{H_2})^{1/2} \quad [21]$$

$$\phi_{eq,4,T} = (U_4^\theta - U_{RE}^\theta) + (T - T_0)\left(\frac{dU_4^\theta}{dT} - \frac{dU_{RE}^\theta}{dT}\right) - \frac{RT}{F}\ln(c_{H_2})^{1/2} \quad [22]$$

$$\phi_{eq,7,T} = (U_7^\theta - U_{RE}^\theta) + (T - T_0)\left(\frac{dU_7^\theta}{dT} - \frac{dU_{RE}^\theta}{dT}\right) + \frac{3RT}{2F}\ln\left(\frac{c_\gamma}{c_{\beta_+}}\right) - \frac{RT}{F}\ln(c_e) \quad [23]$$

$$\phi_{eq,8,T} = (U_8^\theta - U_{RE}^\theta) + (T - T_0)\left(\frac{dU_8^\theta}{dT} - \frac{dU_{RE}^\theta}{dT}\right) + \frac{3RT}{5F}\ln\left(\frac{c_\gamma}{c_\alpha}\right) - \frac{2RT}{5F}\ln(c_e) \quad [24]$$

In the above equations, U_{RE}^θ is the standard potential of the Hg/HgO reference electrode *vs.* the standard hydrogen electrode (SHE). The temperature dependence of equilibrium potentials has also been included in the above equations.

The oxygen reduction on the platimum electrode is mass-transfer limited due to the huge driving force for this reaction on the platinum electrode. The rate of this reaction is expressed in a limiting-current equation

$$j_5 = -i_{5,ref,T_0}\left(\frac{c_{O_2}}{c_{O_2,ref}}\right)\exp\left[-\frac{\Delta E_{a,5}}{R}\left(\frac{1}{T} - \frac{1}{T_0}\right)\right] \quad [25]$$

The conversion from α-$Ni(OH)_2$ to β-$Ni(OH)_2$ is assumed to be a first order chemical reaction, which gives

$$j_6 = i_{6,ref,T_0}\left(\frac{c_\alpha}{c_{\alpha,ref}}\right)\exp\left[-\frac{\Delta E_{a,6}}{R}\left(\frac{1}{T} - \frac{1}{T_0}\right)\right] \quad [26]$$

Hysteresis potential behavior exists for nickel reactions, *i.e.*, the apparent open-circuit potential of the discharge process is lower than that of the charge process. In this work, for the discharge processes of reactions Eq. 1, 7, and 8, smaller values of the equilibrium potential than those for the charge processes have been used. The governing equations of the model are presented subsequently. The diffusion in the gas phase has been neglected because it is much faster than that in the liquid phase.

Nickel electrode.—The material balance of the KOH electrolyte is expressed by

$$\varepsilon_{pos,l}\frac{\partial c_e}{\partial t} - \varepsilon_{pos,l}^{1.5}\frac{\partial}{\partial x}\left(D_e\frac{\partial c_e}{\partial x}\right) - \frac{t_-^*}{F}\frac{\partial i_l}{\partial x} + \frac{a_{pos}}{F} \times \left(j_1 + j_2 + j_3 + 2j_7 + \frac{7}{5}j_8\right) = 0 \quad [27]$$

Modified Ohm's law in the electrolyte is

$$i_l = -\varepsilon_{pos,l}^{1.5}\kappa_e \frac{\partial \phi_1}{\partial x} - \frac{2RT}{F}\varepsilon_{pos,l}^{1.5}\kappa_e\left(1 + \frac{d\ \ln\ f_{\pm}}{d\ \ln\ c_e}\right) \times \left[1 - \left(1 + 2\frac{c_e}{c_0}\right)t_-^* + \frac{1}{2}\frac{c_e}{c_0}\right]\frac{\partial\ \ln\ c_e}{\partial x} \quad [28]$$

The conservation of charge in the electrolyte gives

$$\frac{\partial i_l}{\partial x} = a_{pos}(j_1 + j_2 + j_3 + j_7 + j_8) \quad [29]$$

The mass balances of nickel species are given by

$$l_y\frac{dc_{\beta_-}}{dt} = \frac{-j_1 + j_6}{F} \quad [30]$$

$$l_y\frac{dc_{\beta_+}}{dt} = \frac{j_1 - 3j_7/2}{F} \quad [31]$$

$$l_y\frac{dc_{\gamma}}{dt} = \frac{3j_8/5 + 3j_7/2}{F} \quad [32]$$

Only the concentrations of three phases are accounted for in the model, and that of the left phase can be obtained from the following mass balance

$$c_\alpha = c_{H^+,max} - (c_{\beta_-} + c_{\beta_+} + c_\gamma) \quad [33]$$

The boundary conditions at the back of the nickel electrode are

$$-\varepsilon_{pos,l}^{1.5} D_e \frac{\partial c_e}{\partial x}\bigg|_{x=0} = 0 \quad [34]$$

$$-\varepsilon_{pos,l}^{1.5} \kappa_e \frac{\partial \phi_1}{\partial x}\bigg|_{x=0} = 0 \quad [35]$$

$$i_l|_{x=0} = 0 \quad [36]$$

The boundary conditions at the interface between the nickel electrode and the separator are

$$-\varepsilon_{pos,l}^{1.5} D_e \frac{\partial c_e}{\partial x}\bigg|_{x=l_{pos}^-} = -\varepsilon_{sep,l}^{1.5} D_e \frac{\partial c_e}{\partial x}\bigg|_{x=l_{pos}^+} \quad [37]$$

$$-\varepsilon_{pos,l}^{1.5} \kappa_e \frac{\partial \phi_l}{\partial x}\bigg|_{x-l_{pos}^-} = -\varepsilon_{sep,l}^{1.5} \kappa_e \frac{\partial \phi_1}{\partial x}\bigg|_{x=l_{pos}^+} \quad [38]$$

$$i_l|_{x=l_{pos}^-} = i_{app} \quad [39]$$

Separator.—The material balance of the KOH electrolyte is expressed by

$$\varepsilon_{sep,l}\frac{\partial c_e}{\partial t} - \varepsilon_{sep,l}^{1.5}\frac{\partial}{\partial x}\left(D_e\frac{\partial c_e}{\partial x}\right) = 0 \quad [40]$$

Modified Ohm's law in the electrolyte is

$$i_{app} = -\varepsilon_{sep,l}^{1.5}\kappa_e \frac{\partial \phi_1}{\partial x} - \frac{2RT}{F}\varepsilon_{sep,l}^{1.5}\kappa_e\left(1 + \frac{d\ \ln\ f_{\pm}}{d\ \ln\ c_e}\right) \times \left[1 - \left(1 + 2\frac{c_e}{c_0}\right)t_-^* + \frac{1}{2}\frac{c_e}{c_0}\right]\frac{\partial\ \ln\ c_e}{\partial x} \quad [41]$$

The conservation of charge in the electrolyte gives

$$i_l = i_{app} \quad [42]$$

The boundary conditions at the interface between the separator and platinum electrode are

$$-\varepsilon_{sep,l}^{1.5} D_e \frac{\partial c_e}{\partial x}\bigg|_{x=l_{pos}+l_{sep}} + \frac{t_-^*}{F} i_{app} = i_{app} \quad [43]$$

$$i_{app} = -\varepsilon_{sep,l}^{1.5}\kappa_e \frac{\partial \phi_l}{\partial x}\bigg|_{x=l_{pos}+l_{sep}} \quad [44]$$

Platinum electrode.—The conservation of charge gives

$$-i_{app} = a_{neg} l_{neg}(j_4 + j_5) \quad [45]$$

Whole cell.—The cell potential that includes the effect of the internal electric resistance from metal leads and electrode substrates is

$$V_{cell} = \phi_{pos} - \phi_{neg} + i_{cell}R_{cell} \quad [46]$$

The mass balances of hydrogen and oxygen gases are given by

$$\frac{dn_{H_2}}{dt} = N_{module}\pi(r_{out}^2 - r_{in}^2)\frac{a_{pos}l_{pos}j_3 + a_{neg}l_{neg}j_4}{2F} \quad [47]$$

$$\frac{dn_{O_2}}{dt} = N_{module}\pi(r_{out}^2 - r_{in}^2)\frac{a_{pos}l_{pos}j_2 + a_{neg}l_{neg}j_5}{4F} \quad [48]$$

where

$$n_{H_2} = \frac{p_{H_2}V_{gas}}{RT} = c_{H_2}^g V_{gas} \quad [49]$$

$$n_{O_2} = \frac{p_{O_2}V_{gas}}{RT} = c_{O_2}^g V_{gas} \quad [50]$$

Equilibrium is assumed to exist between the gas phase and the dissolved phase hydrogen and oxygen; then from Henry's law, there is

$$c_{H_2} = \frac{c_{H_2}^g}{K_{O_2}} \quad [51]$$

$$c_{O_2} = \frac{c_{O_2}^g}{K_{O_2}} \quad [52]$$

The cell pressure is expressed by

$$P_{cell} = \frac{(n_{H_2} + n_{O_2})RT}{V_{gas}} \quad [53]$$

The energy balance of the whole cell is given by

$$m_{cell}c_{p,cell}\frac{dT}{dt} = -h_{cell}A_{vessel}(T - T_a) + \dot{q} \quad [54]$$

The heat generation rate of the cell is described with

$$\dot{q} = V_{gas}\frac{dP_{cell}}{dt} + i_{cell}R_{cell}^2 + N_{module}\pi(r_{out}^2 - r_{in}^2) \times \left[i_{app}(\phi_{pos} - \phi_{neg}) - \left(\sum_{k=1,2,3,7,8} a_{pos}l_{pos}j_k(U_k - T)\frac{dU_k}{dT} + \sum_{k=4,5} a_{neg}l_{neg}j_k(U_k - T)\frac{dU_k}{dT} \right) \right] \quad [55]$$

where

$$\frac{dP_{cell}}{dt} = \left(\frac{dn_{H_2}}{dt} + \frac{dn_{O_2}}{dt} \right)\frac{RT}{V_{gas}} + \frac{(n_{H_2} + n_{O_2})R}{V_{gas}}\frac{dT}{dt} \quad [56]$$

In the above equation, the temperature is assumed to be uniform inside the cell, and the heat effect of the chemical reaction Eq. 6 is neglected.

Due to the limited rate of heat transfer, temperature differences exist inside a nickel-hydrogen cell. If the temperature difference between different portions of the cell is high enough, water transport through the evaporation and condensation mechanism could happen. This may significantly affect cell performance.[4,5] To investigate such possibilities, the heat transfer in the radial direction of the cell stack is modeled, as given by the following governing equations

$$\rho_{stack}c_{p,cell}\frac{\partial T_{stack}}{\partial t} = \lambda_{stack}\frac{1}{r}\frac{d}{dr}\left(r\frac{dT_{stack}}{dr} \right) + \frac{\dot{q}}{N_{module}\pi(r_{out}^2 - r_{in}^2)} \quad [57]$$

with boundary conditions

$$-\lambda_{stack}\frac{dT_{stack}}{dr}\bigg|_{r=r_{in}} = 0 \quad [58]$$

$$-\lambda_{stack}\frac{dT_{stack}}{dr}\bigg|_{r=r_{out}} = h_{stack}(T_{stack} - T_0) \quad [59]$$

The heat transfer through the inner surface as well as that through the upper and lower surfaces of the pineapple-shaped cell stack has been neglected. Some auxiliary equations for the model are listed in the Appendix. There are six dependent variables in the x direction (c_e, ϕ_l, i_l, c_{β_-}, c_{β_+}, and c_γ), one dependent variable in the r direction (T_{stack}), and eight dependent variables that are time-dependent only (V_{cell}, $\dot{q}$, ϕ_{neg}, n_{H_2}, n_{O_2}, $c^g_{H_2}$, $c^g_{O_2}$, and T). The nickel substrate potential, ϕ_{pos}, was set as the reference potential. The model equations were solved with DASRT, an extension of the popular DAEs solver DASSL with discrete event detections. The model program is coded in FORTRAN. A simulation for one process typically takes tens of seconds on a Pentium PC.

Results and Discussion

The model parameters are listed in Table I. The kinetic parameters of reactions are given in Table II. The model predictions are compared to the experimental data (voltage, temperature, and pressure) of a TRW 30 Ah cell for the following processes: C/10 rate charge for 16 h, open-circuit for 1 h, and C/2 rate discharge to the cutoff voltage 0.9 V at three ambient temperatures 0, 10, and 20°C. The C rate is based on the rated capacity of the TRW cell, *i.e.*, it equals 30 A. The cell was fully discharged before the experiment. The positive precharge of a TRW cell is estimated to be around 8% of the nickel active material. Thus, the initial mole fractions of nickel phases were set to be: 0.90 β-$Ni(OH)_2$, 0.07 β-NiOOH, 0.02 α-$Ni(OH)_2$, and 0.01 γ-NiOOH. The initial hydrogen partial pressure was set at 0.1 atm, and oxygen partial pressure at 1×10^{-4} atm. As shown in Fig. 3-5, the comparisons of the model predictions and experimental data show good qualitative agreement. The experimental data were obtained with the cell temperature being tightly controlled, thus a high value of heat transfer coefficient has been used in the model. The detailed analysis of model predictions is given subsequently.

Table I. Model parameters.

Parameter	Value	Source[a]
a_0	2000 cm^2/cm^3	
a_{neg}	1500 cm^2/cm^3	
A_{vessel}	600 cm^2	
C	30 Ah	
$c_{p,cell}$	1.0 J/K g	
h_{cell}	6.0×10^{-3} W/cm^2 K	
h_{stack}	6.0×10^{-3} W/cm^2 K	
l_{neg}	0.02 cm	
l_{pos}	0.0762 cm	
l_{sep}	0.06 cm	
$L_{Ni(OH)_2}$	1.50 g/cm^3 void volume	
m_{cell}	1.2×10^3 g	
$M_{Ni(OH)_2}$	92.7 g/mol	Ref. 3
N_{Module}	24	
r_{in}	1.5875 cm	
r_{out}	4.2926 cm	
R_{cell}	0.5×10^{-3} Ω	
t^*_-	0.78	Ref. 3
V_{gas}	465.0 cm^3	
$\varepsilon_{0,pos}$	0.81	
$\varepsilon_{pos,l}$	0.30	
$\varepsilon_{sep,l}$	0.85	
λ_{stack}	0.1 W/cm K	
$\rho_{Ni(OH)_2}$	3.4 g/cm^3	Ref. 6
ρ_{stack}	2.0 g/cm^3	

[a] The parameters that have no source listed are either assumed values or design parameters.

Figure 3 shows the cell potential at different ambient temperatures. Observe that the charge potential increases as the temperature decreases. This is because reaction rates are slow at low temperatures and high overpotentials are needed to maintain the same charge current. The high plateau in the potential curve corresponds to the overcharge period. The dominant reactions during overcharge are the oxygen evolution on the nickel electrode and the oxygen reduction on the platinum electrode. Since the oxygen evolution is slower than nickel reactions, higher overpotential is needed to maintain the same charge current. The relatively larger change of the overcharge plateau indicates that the oxygen evolution is more sensitive to the temperature change than are the other reactions. The discharge potential curves terminate at different time points. This indicates different cell discharge capacities at different temperatures. The phenomenon of high capacities at low temperatures is contrary to what is expected from the kinetic mechanisms. Low reaction rates at low temperatures would cause a discharge process to reach the cutoff voltage earlier due to high overpotential losses. The real mechanism for this phenomenon will be discussed later.

Figure 4 shows the cell temperature at different ambient temperatures. The cell temperature slightly decreases in the early period of the charge process. This indicates that endothermic heat effects of the cell reactions dominate. As the cell approaches overcharge, the cell temperature rapidly increases because more and more input energy is wasted on the side reactions, *e.g.*, the oxygen evolution on the nickel electrode and the oxygen reduction on the platinum elec-

Table II. Kinetic parameters.

Parameter	Value	Source[a]
$c_{e,ref}$	5.8×10^{-3} mol/cm^3	
$c_{\beta_-,ref}$	$0.5c_{H^+,max}$	
$c_{\beta_+,ref}$	$0.5c_{H^+,max}$	
$c_{\alpha,ref}$	$0.5c_{H^+,max}$	
$c_{\gamma,ref}$	$0.5c_{H^+,max}$	
$i_{o,1,ref,T_0}$	6.1×10^{-5} A/cm^2	Ref. 3
$i_{o,2,ref,T_0}$	1.0×10^{-10} A/cm^2	Ref. 3
$i_{o,3,ref,T_0}$	2.5×10^{-19} A/cm^2	
$i_{0,4,ref,T_0}$	1.0×10^{-4} A/cm^2	
$i_{o,5,ref,T_0}$	1.0×10^{-4} A/cm^2	
$i_{o,6,ref,T_0}$	1.0×10^{-6} A/cm^2	
$i_{o,7,ref,T_0}$	2.0×10^{-7} A/cm^2	
$i_{o,8,ref,T_0}$	6.1×10^{-5} A/cm^2	
$P_{H_2,ref}$	1 atm	
$P_{O_2,ref}$	1 atm	
T_0	298.15 K	
U^{θ}_{Re}	0.0983 V	Ref. 19
U^{θ}_1	0.5183 V	Ref. 19
U^{θ}_2	0.4011 V	Ref. 19
U^{θ}_3	−0.8280 V	Ref. 19
U^{θ}_4	−0.8280 V	Ref. 19
U^{θ}_5	0.4011 V	Ref. 19
U^{θ}_7	0.5783 V	
U^{θ}_8	0.4783 V	
ΔU^{θ}_1	0.10 V	Ref. 10
ΔU^{θ}_7	0.06 V	
ΔU^{θ}_8	0.06 V	Ref. 10
$\frac{dU^{\theta}_{RE}}{dT}$	−1.125 mV/K	Ref. 19
$\frac{dU^{\theta}_1}{dT}$	−1.35 mV/K	Ref. 19
$\frac{dU^{\theta}_2}{dT}$	−1.6816 mV/K	Ref. 19
$\frac{dU^{\theta}_3}{dT}$	−0.836 mV/K	Ref. 19
$\frac{dU^{\theta}_4}{dT}$	−0.836 mV/K	Ref. 19
$\frac{dU^{\theta}_5}{dT}$	−1.6816 mV/K	Ref. 19
$\frac{dU^{\theta}_7}{dT}$	−1.35 mV/K	
$\frac{dU^{\theta}_8}{dT}$	−1.35 mV/K	
$\alpha_{a,1}$	0.5	Ref. 3
$\alpha_{c,1}$	0.5	Ref. 3
$\alpha_{a,2}$	1.25	Ref. 3
$\alpha_{c,2}$	0.75	Ref. 3
$\alpha_{a,3}$	0.5	Ref. 3
$\alpha_{c,3}$	0.5	Ref. 3
$\alpha_{a,4}$	0.5	Ref. 3
$\alpha_{c,4}$	0.5	Ref. 3
$\alpha_{a,7}$	0.33	
$\alpha_{c,7}$	0.33	
$\alpha_{a,8}$	0.83	
$\alpha_{c,8}$	0.83	
$\Delta E_{a,1}$	10 kJ/mol	
$\Delta E_{a,2}$	120 kJ/mol	
$\Delta E_{a,3}$	150 kJ/mol	
$\Delta E_{a,4}$	10 kJ/mol	
$\Delta E_{a,5}$	10 kJ/mol	
$\Delta E_{a,6}$	10 kJ/mol	
$\Delta E_{a,7}$	10 kJ/mol	
$\Delta E_{a,8}$	10 kJ/mol	

[a] The parameters that have no source listed are assumed values.

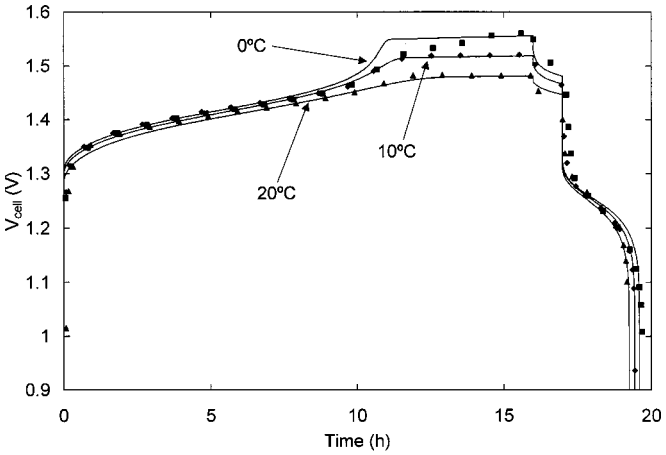

Figure 3. Comparison of the model-predicted cell potential with experimental data of a TRW 30 Ah cell (Ref. 20).

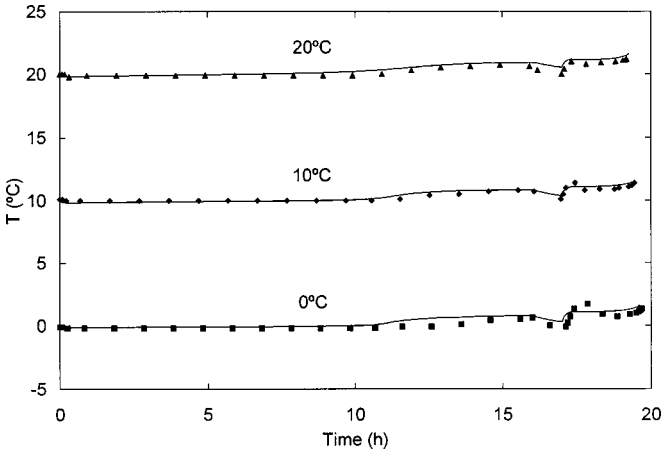

Figure 4. Comparison of the model-predicted cell temperature with experimental data of a TRW 30 Ah cell (Ref. 20).

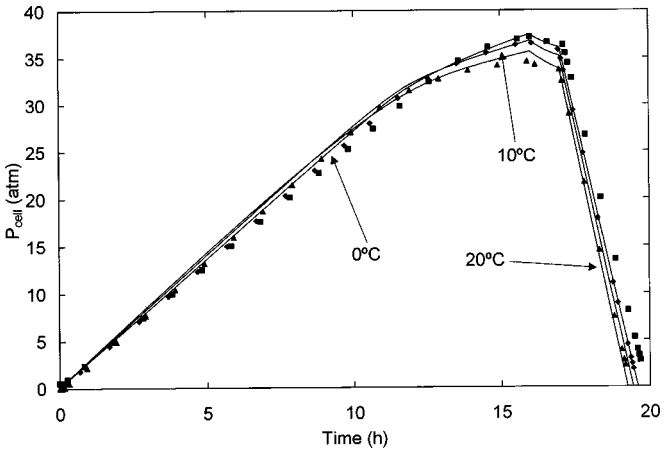

Figure 5. Comparison of the model-predicted cell pressure with experimental data of a TRW 30 Ah cell (Ref. 20).

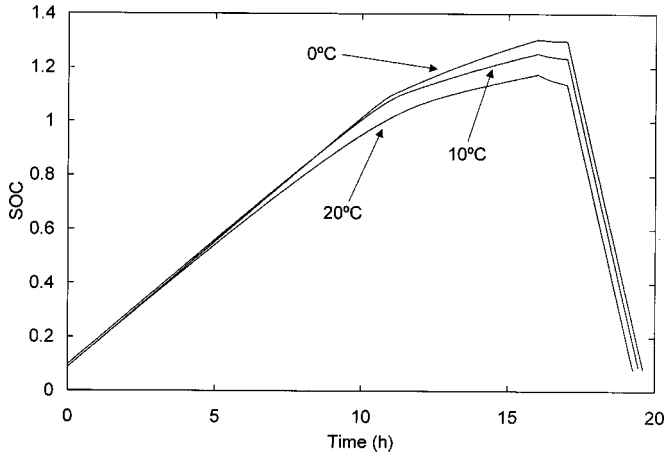

Figure 6. The model-predicted cell SOC.

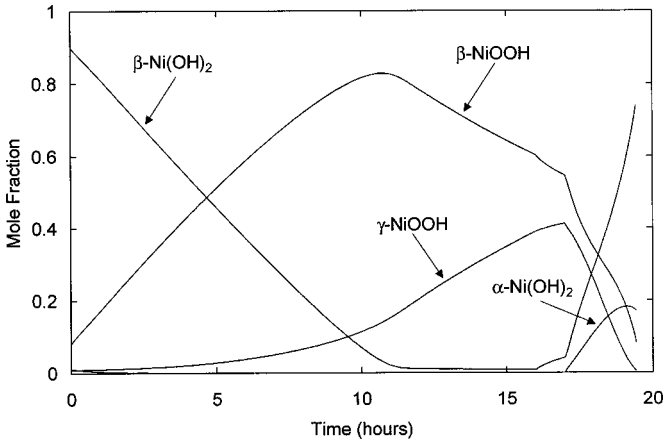

Figure 8. The model-predicted nickel phase distribution (averaged in the nickel electrode) at 10°C ambient temperature.

trode. The cell temperature during discharge is higher than that during overcharge. This is mainly due to high ohmic and overpotential losses with the high current rate (*i.e.*, C/2 *vs.* C/10). At the end of the discharge process, the cell temperature increases rapidly. It is caused by significant overpotential losses when the active reactants are depleted.

Figure 5 shows the cell pressure at different ambient temperatures. With the input of the charge current, hydrogen gas is generated on the platinum electrode and the cell pressure is increased. Since oxygen gas evolved on the nickel electrode will diffuse to the platinum electrode and be reduced there, some charge current on the platinum electrode is wasted on the oxygen reduction. The hydrogen oxidation on the nickel electrode also consumes some generated hydrogen gas and thus reduces the charge efficiency. The cell pressure curve levels off during the overcharge period because a large portion of the charge current goes into the oxygen evolution on the nickel electrode and the oxygen reduction on the platimum electrode, and the hydrogen gas generation becomes insignificant. The pressure curves show different slopes in the early period of the charge process. This is the temperature effect, *i.e.*, the same amount of hydrogen gas gives a low pressure at a low temperature. High cell pressures at the end of the charge process at low temperatures indicate that more hydrogen is generated and thus larger cell capacities are obtained at low temperatures.

Figure 6 shows the predicted cell SOC at different ambient temperatures. It is clear that high cell SOCs are obtained at low temperatures. The SOC curves at different ambient temperatures diverge mainly during the overcharge period. The cell SOC increases faster at lower temperatures. The higher-than-one SOCs indicate that a high nickel oxidation state is present. There is good similarity between the pressure curves in Fig. 5 and the SOC curves in Fig. 6. Thus, the cell pressure can be used as a rough indication of the cell SOC, which is a fact that has been commonly used for a nickel-hydrogen cell.

The predicted nickel phase distribution at different ambient temperatures is shown in Fig. 7-9. Some similar trends are observed in these figures. During the charge process, the amount of β-$Ni(OH)_2$ gradually decreases while that of γ-NiOOH gradually increases. The amount of β-NiOOH increases at first and then it decreases during the overcharge period. During the open-circuit process, the amount of β-NiOOH decreases while that of β-$Ni(OH)_2$ and γ-NiOOH increases. During the discharge process, both the amount of β-NiOOH and γ-NiOOH decreases while that of β-$Ni(OH)_2$ increases. The amount of α-$Ni(OH)_2$ increases at first and then it decreases during the discharge process. However, the quantitative phase distribution is different at different temperatures, *e.g.*, there is comparatively more γ-NiOOH generated during the charge process and more α-$Ni(OH)_2$ generated during the discharge process at low temperatures.

The predicted partial currents of reactions are presented in Fig. 10-18. As shown in Fig. 10, 13, and 16, in the early period of the charge process, the main reactions are the β-$Ni(OH)_2$ to β-NiOOH conversion (Eq. 1) and the hydrogen generation (Eq. 4) while the

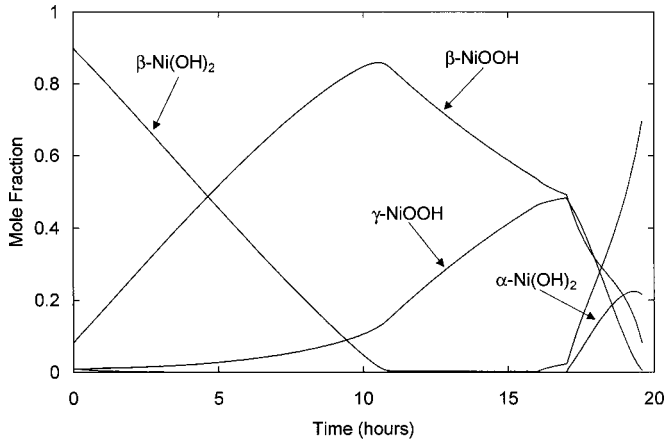

Figure 7. The model-predicted nickel phase distribution (averaged in the nickel electrode) at 0°C ambient temperature.

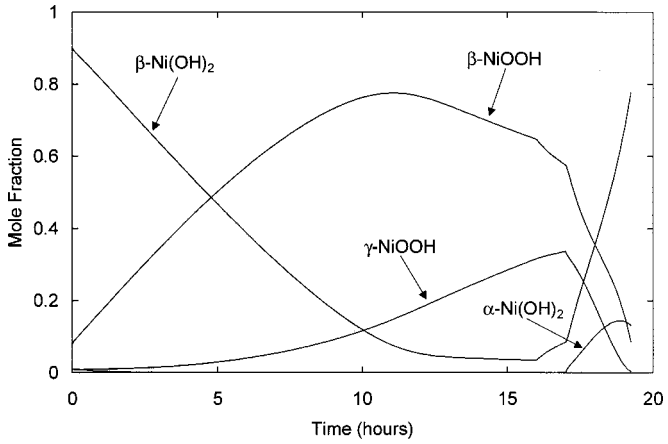

Figure 9. The model-predicted nickel phase distribution (averaged in the nickel electrode) at 20°C ambient temperature.

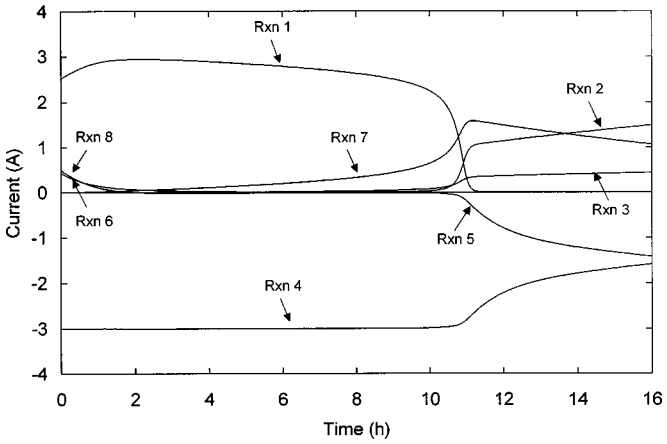

Figure 10. Model-predicted partial currents during the charge process at 0°C ambient temperature.

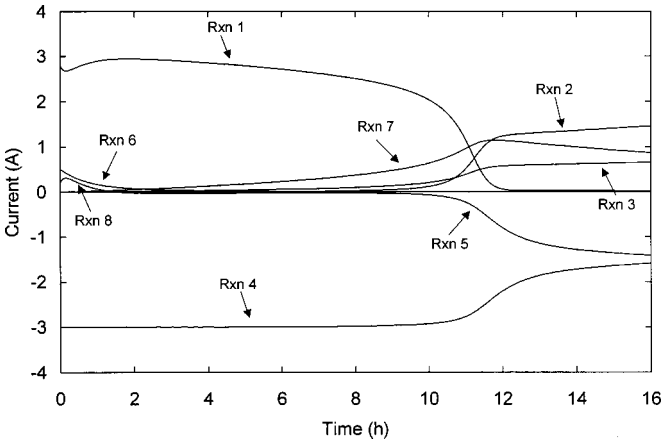

Figure 13. Model-predicted partial currents during the charge process at 10°C ambient temperature.

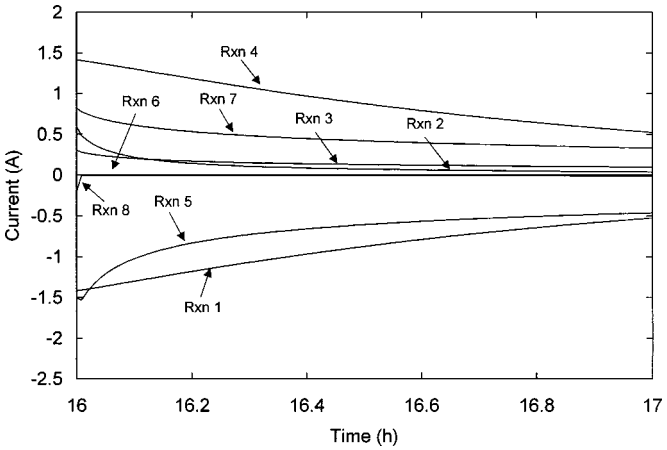

Figure 11. Model-predicted partial currents during the open-circuit process at 0°C ambient temperature.

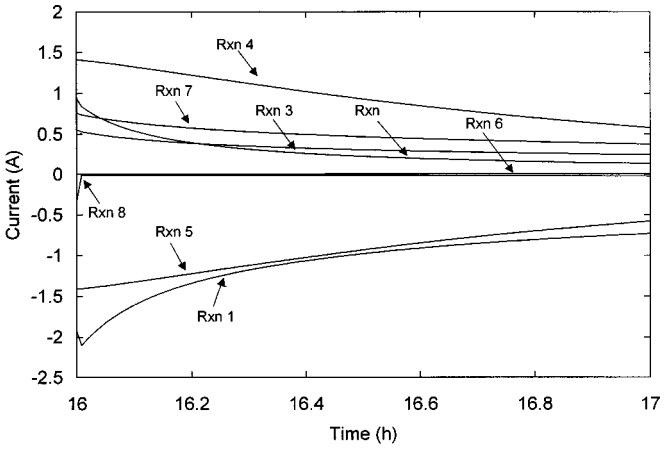

Figure 14. Model-predicted partial currents during the open-circuit process at 10°C ambient temperature.

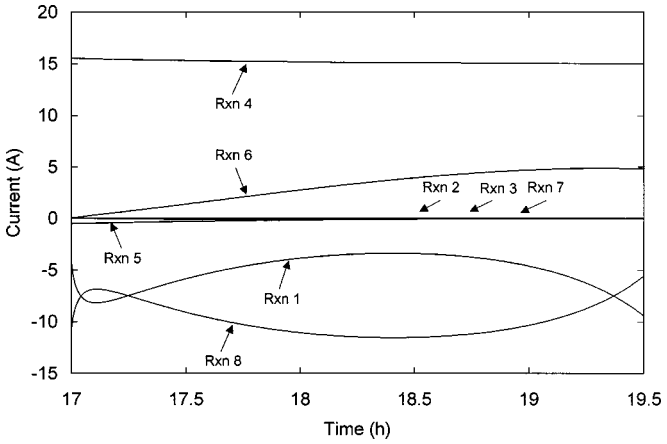

Figure 12. Model-predicted partial currents during the discharge process at 0°C ambient temperature.

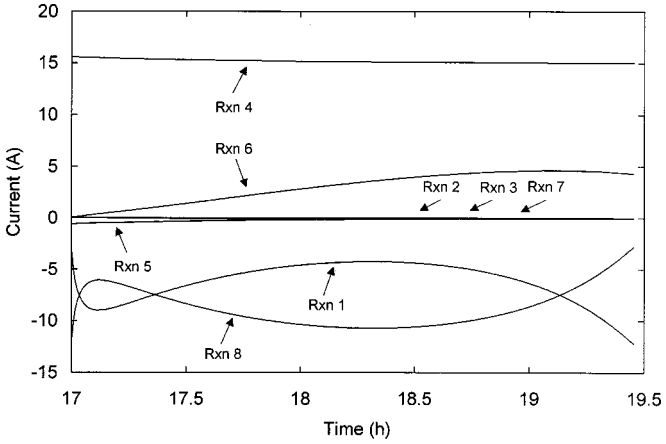

Figure 15. Model-predicted partial currents during the discharge process at 10°C ambient temperature.

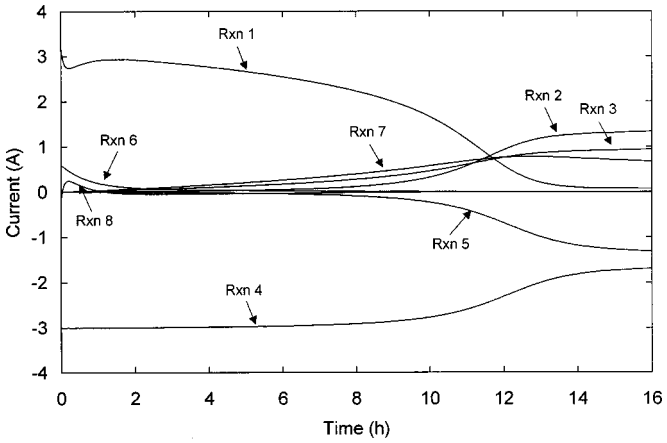

Figure 16. Model-predicted partial currents during the charge process at 20°C ambient temperature.

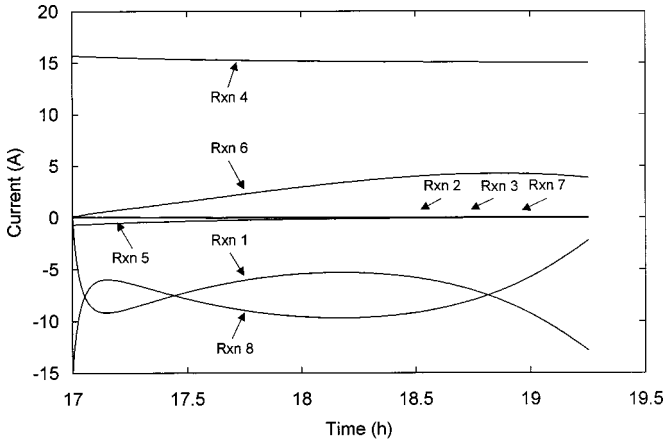

Figure 18. Model-predicted partial currents during the discharge process at 20°C ambient temperature.

side reactions on both electrodes are negligible. During the overcharge period, the oxygen evolution (Eq. 2), the hydrogen oxidation (Eq. 3), the oxygen reduction (Eq. 5), and the β-NiOOH to γ-NiOOH conversion (Eq. 7) become significant while the β-$Ni(OH)_2$ to β-NiOOH conversion (Eq. 1) becomes negligible. At high temperatures, the time when the oxygen evolution (Eq. 2), the hydrogen oxidation (Eq. 3), and the oxygen reduction (Eq. 5) are significant comes earlier, which indicates lower charge efficiency at high temperatures. It is observed that the partial current of the β-NiOOH to γ-NiOOH conversion (Eq. 7) is higher at lower temperatures. In fact, it is higher than that of the oxygen evolution (Eq. 2) and the hydrogen oxidation (Eq. 3) in the early overcharge period at 0°C but it is lower during most of the overcharge period at 20°C. The mechanism of the cell capacity variation at different temperatures is clearly shown to be the competition between nickel reactions and side reactions. At high temperatures, the oxygen evolution (Eq. 2) and the hydrogen oxidation (Eq. 3) on the nickel electrode can be so fast that the β-$Ni(OH)_2$ to β-NiOOH conversion (Eq. 1) will be affected. While at low temperatures, the oxygen evolution (Eq. 2) and the hydrogen oxidation (Eq. 3) are so sluggish that the β-NiOOH to γ-NiOOH conversion (Eq. 7) will be favored. Consequently high charge efficiencies and thus high final cell SOCs will be obtained at low temperatures.

As shown in Fig. 11, 14, and 17, during the open-circuit period, there is significant self-discharge at all three ambient temperatures. On the nickel electrode β-NiOOH is discharged to β-$Ni(OH)_2$ (Eq. 1), which drives the β-NiOOH to γ-NiOOH conversion (Eq. 7), the oxygen evolution (Eq. 2) and the hydrogen oxidation (Eq. 3). On the platinum electrode, oxygen is reduced (Eq. 5) while hydrogen is oxidized (Eq. 4). One interesting result is that the self-discharge currents of the nickel electrode and hydrogen electrode can be different. In fact, the self-discharge current on the platinum electrodes is larger than that on the nickel electrode at 0°C and the converse is true at 20°C. The self-discharge currents on both electrodes are larger at high temperatures.

As shown in Fig. 12, 15, and 18, during the discharge process, the main reactions are the β-NiOOH to β-$Ni(OH)_2$ conversion (Eq. 1), the γ-NiOOH to α-$Ni(OH)_2$ conversion (Eq. 8), the α-$Ni(OH)_2$ to β-$Ni(OH)_2$ conversion (Eq. 6), and the hydrogen oxidation Eq. (4), while other reactions (Eq. 2, 3, 5, and 7) are insignificant. Both β-NiOOH and γ-NiOOH are consumed and both β-$Ni(OH)_2$ and α-$Ni(OH)_2$ are generated during discharge. Some generated α-$Ni(OH)_2$ converts to β-$Ni(OH)_2$ quickly and thus β-$Ni(OH)_2$ is the dominant phase in the discharged nickel active material. It is observed that the β-NiOOH to β-$Ni(OH)_2$ conversion (Eq. 1) and the γ-NiOOH to α-$Ni(OH)_2$ conversion (Eq. 8) provides two parallel reduction paths for the nickel active material. The partial currents of these two reactions change dramatically during the discharge process. At first, the partial current of the γ-NiOOH to α-$Ni(OH)_2$ conversoin is larger. Then the partial current of the β-NiOOH to β-$Ni(OH)_2$ conversion becomes larger. Later on, the partial current of the γ-NiOOH to α-$Ni(OH)_2$ conversion is larger again. Finally,

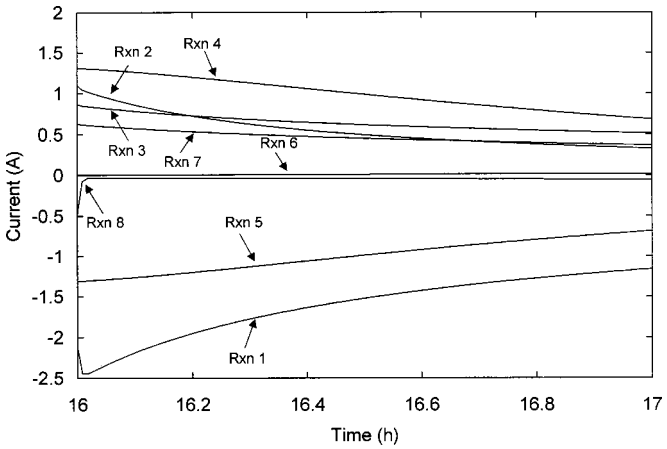

Figure 17. Model-predicted partial currents during the open-circuit process at 20°C ambient temperature.

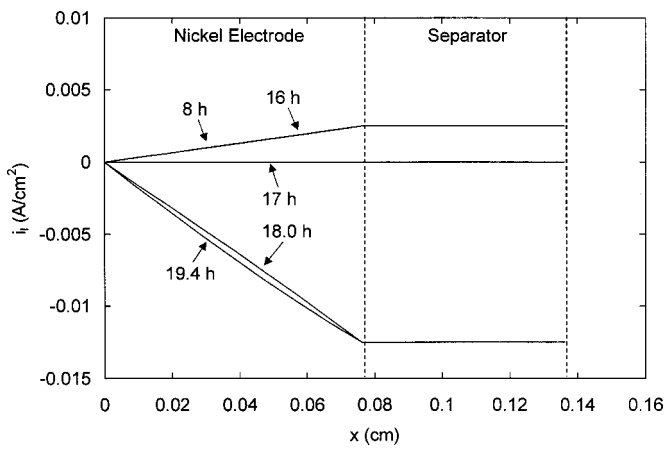

Figure 19. The model-predicted liquid phase current density profile across the cell module at 10°C ambient temperature.

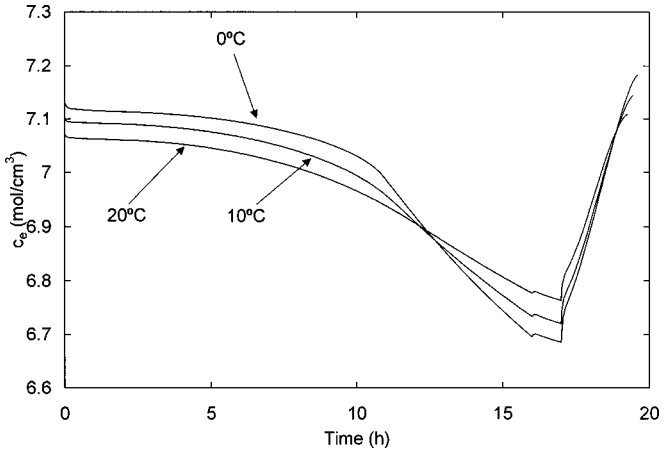

Figure 20. The model-predicted average KOH concentration.

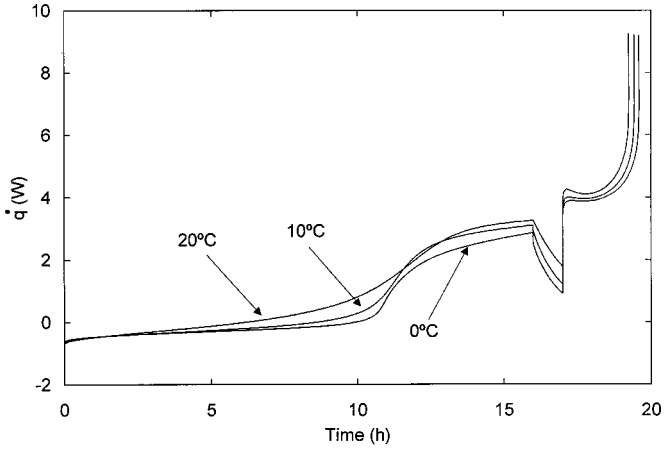

Figure 22. The model-predicted heat generation rate of the cell.

the partial current of the β-NiOOH to β-$Ni(OH)_2$ conversion becomes dominant. At low temperatures, the partial current differences of these two reactions are more prominent.

Figure 19 shows the predicted liquid phase current density at several time points at 10°C ambient temperature. The constant line in the separator means that the whole applied current density passes through the separator unchanged. In the nickel electrode, almost linear lines are obtained during both the charge and discharge processes. This indicates that reactions occur almost uniformly in the nickel electrode. Thus, the nickel active material is almost uniformly utilized in the nickel electrode, and the nickel phase distribution is similar at all locations across the nickel electrode.

Figure 20 shows the predicted average KOH concentration at different ambient temperatures. During the charge process, KOH is taken up into the nickel active material with the β-NiOOH to γ-NiOOH conversion (Eq. 1). This causes the decrease of the KOH concentration during the charge process. Since the β-NiOOH to γ-NiOOH conversion is more significant during the overcharge period, KOH concentration decreases rapidly at the same time. During the discharge process, KOH is released back to the electrolyte with the γ-NiOOH to α-NiOOH conversion (Eq. 8) and the KOH concentration is restored. A similar KOH concentration change has been observed experimentally.[1] The model predicts that there is comparatively a larger variation of the KOH concentration at low temperatures, which is directly related to the amount of γ-NiOOH generated and consumed.

Figure 21 shows the predicted KOH concentration profile at several time points at 10°C ambient temperature. During the charge process, OH^- ion is consumed in the nickel electrode and generated in the platinum electrode, thus the KOH concentration changes from low values in the nickel electrode to high values in the platinum electrode. During the discharge process, the converse holds. The difference of KOH concentration across the cell module is actually not very significant and it is less than 5% during the C/2 discharge.

Figure 22 shows the predicted heat generation rate of the cell at different ambient temperatures. The heat generation rate is negative during the early period of the charge process. It increases rapidly near the overcharge period. During the overcharge period, a big portion of the input energy is wasted on side reactions, which causes a high heat generation rate. In fact, it can be expected that when the nickel active material is fully charged, the whole input energy will become heat generation. It is interesting to note that there is significant heat generation during the open-circuit period. This indicates that significant self-discharge occurs. The heat generation rate during the discharge process is higher than that during the overcharge period, which is mainly caused by the comparatively higher rate of the discharge process. The heat generation rate shoots up to very high values at the end of the discharge process. This may lead to thermal safety problems. To avoid such hazard situations, the discharge process needs to be terminated earlier with high cutoff values.

Figure 23 shows the temperature difference in the cell stack at different ambient temperatures. At the early period of the charge process, the inner portion of the cell stack has lower temperature than the outer portion due to the endothermic heat effects; however,

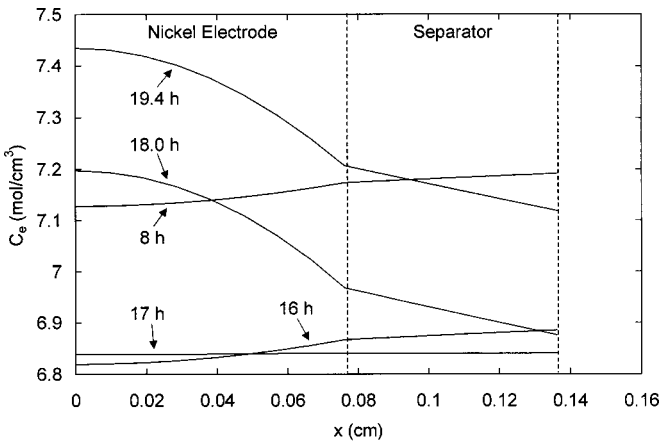

Figure 21. The model-predicted KOH concentration profile across the cell module at 10°C ambient temperature.

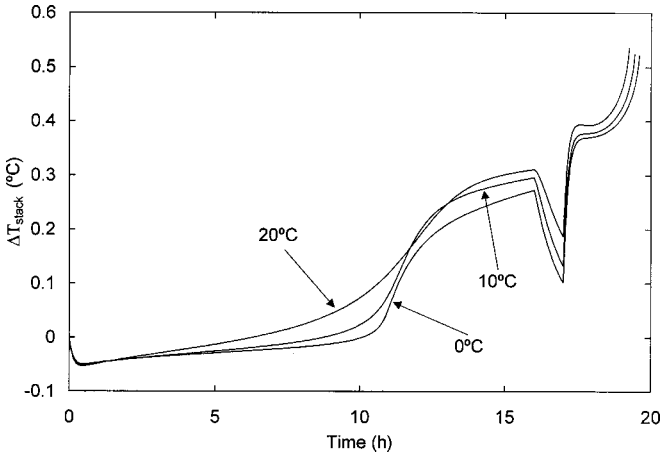

Figure 23. The model-predicted temperature difference in the cell stack.

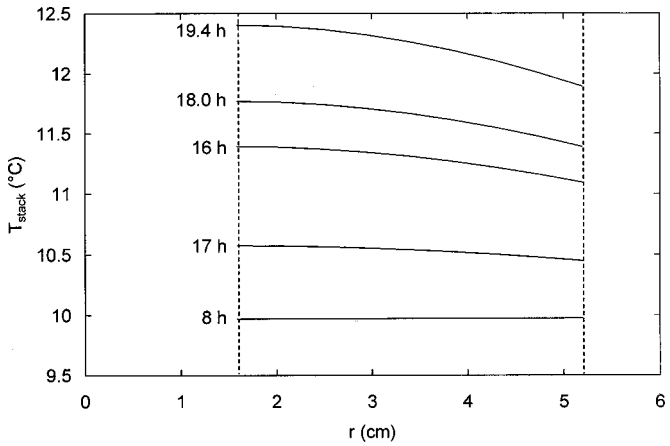

Figure 24. The model-predicted temperature profile in the radial direction of the cell stack at 10°C ambient temperature.

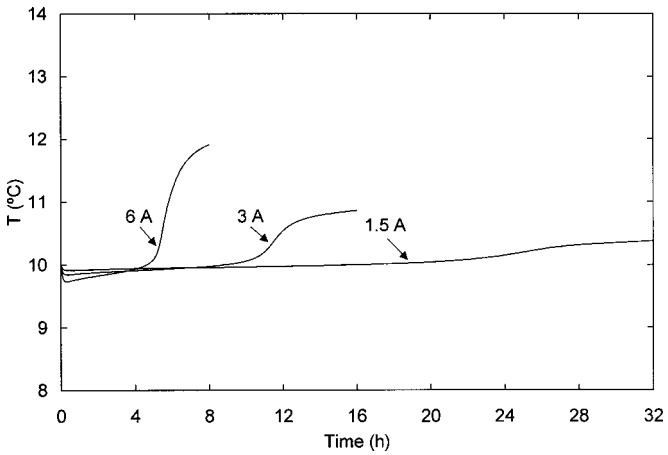

Figure 26. The model-predicted cell temperature at different charge rates at 10°C ambient temperature.

the temperature difference is not significant. During the overcharge and discharge processes, the inner portion of the cell stack has higher temperature than the outer portion due to the significant heat generation in the cell stack; however, the value of temperature difference is still not large enough to cause water transport through the evaporation and condensation mechanism. The predicted temperature profiles across the radial direction of the cell stack at different time points are given in Fig. 24. It is observed that the temperature difference in the cell stack is always less than 1°C for the simulated processes. Thus the assumption of uniform cell temperature seems to be reasonable.

Figures 25-28 show the simulation results for the charge process at different rates (C/20 for 32, C/10 for 16, and C/5 for 4 h). The same total amount of charge has been used for these processes. As shown in Fig. 25, high charge cell potentials are needed at high charge rates. This is due to high ohmic and overpotential losses at high charge rates. As shown in Fig. 26, the cell temperature varies more significantly at high charge rates. Cell temperature decreases deeper in the early period of the charge process, and reaches higher during the overcharge period. As shown in Fig. 27, the slope of the cell pressure curve varies with the charge rate. High rates increase the cell pressure to the same value in less time and cause the slope of the cell pressure curve to be steeper. The final cell pressures for the three rates are similar. However, as shown in Fig. 28, there is some difference in the final cell SOCs. Low charge rates are pre-

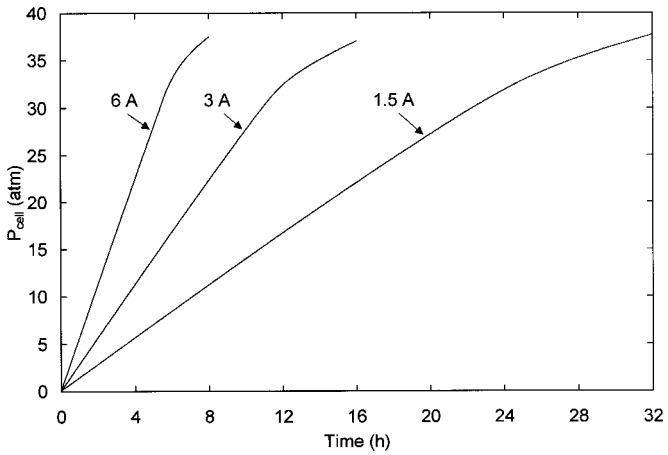

Figure 27. The model-predicted cell pressure at different charge rates at 10°C ambient temperature.

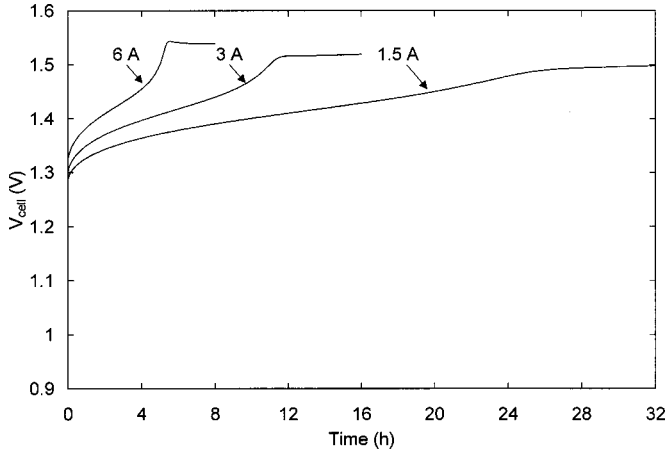

Figure 25. The model-predicted cell potential at different charge rates at 10°C ambient temperature.

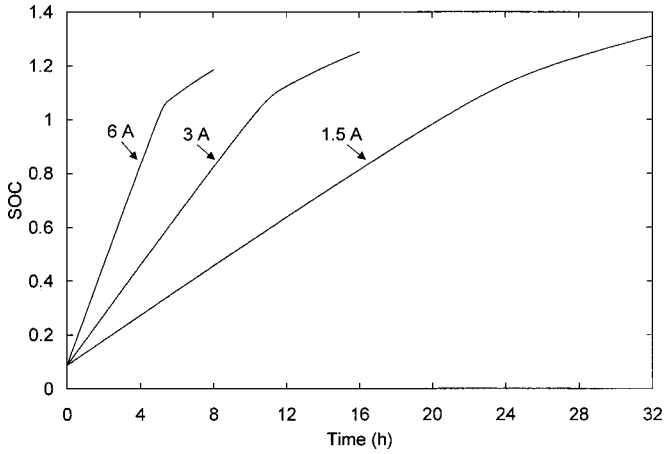

Figure 28. The model-predicted cell SOC at different charge rates at 10°C ambient temperature.

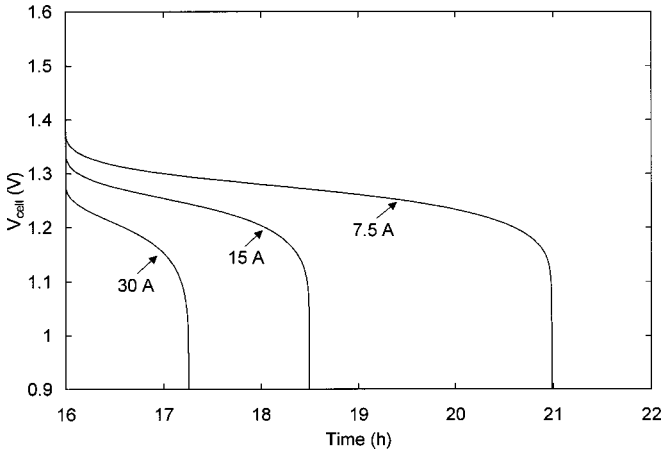

Figure 29. The model-predicted cell potential at different discharge rates at 10°C ambient temperature.

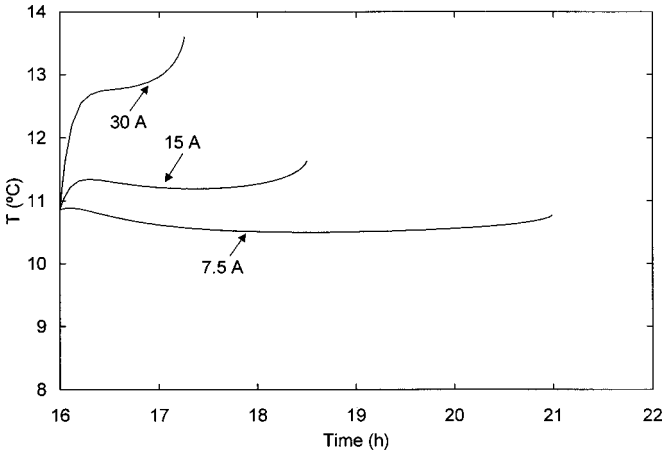

Figure 30. The model-predicted cell temperature at different discharge rates at 10°C ambient temperature.

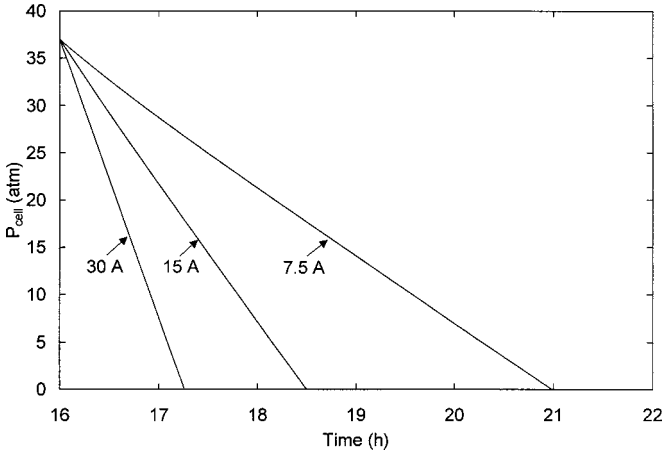

Figure 31. The model-predicted cell pressure at different discharge rates at 10°C ambient temperature.

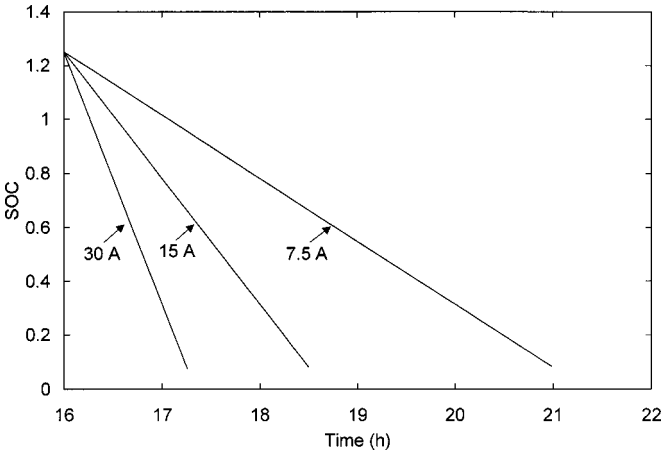

Figure 32. The model-predicted cell SOC at different discharge rates at 10°C ambient temperature.

dicted to yield high final cell SOCs. This could be the effect of low cell temperatures during overcharge at low charge rates, *i.e.*, the side reactions are slower at low cell temperatures.

Figures 29-32 show the simulation results for the discharge process at different rates (C, C/2, and C/4 to the same cutoff voltage, 0.9 V). The initial condition is set to be the ending state of the C/10 charge process for 16 h. As shown in Fig. 29 high discharge rates cause low discharge cell potentials. It is due to high ohmic and overpotential losses at high discharge rates. As shown in Fig. 30, the cell temperature is higher at high discharge rates. In fact, the cell temperature at the C/20 discharge rate decreases from the initial value, which indicates that the heat generation rate at that discharge rate is lower than that during C/10 overcharge. As shown in Fig. 27, the slope of the cell pressure curve varies with the discharge rate. High rates decrease the cell pressure to the same value in less time and cause the slope of the cell pressure curve to be steeper. As shown in Fig. 28, the final discharged cell SOCs are almost the same for the three cases.

Figure 33-36 show the model predictions at three different heat transfer coefficients for the following processes: C/10 charge for 16 h, open circuit for 1 h, and C/2 discharge to the cutoff voltage, 0.9 V. As shown in Fig. 33, cell potential curves in three cases are similar in the early period of the charge process. However, there is a significant difference in the cell potential during the overcharge period. For the adiabatic process, the cell potential rises first and then sharply drops to very low values. As shown in Fig. 34, the cell

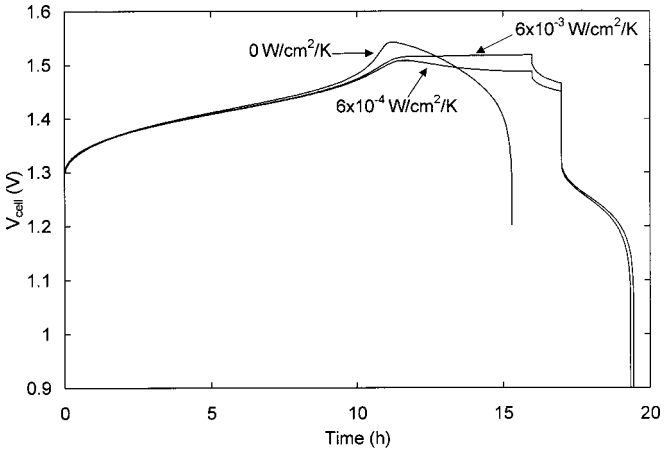

Figure 33. The model-predicted cell potential at different heat transfer conditions at 10°C ambient temperature.

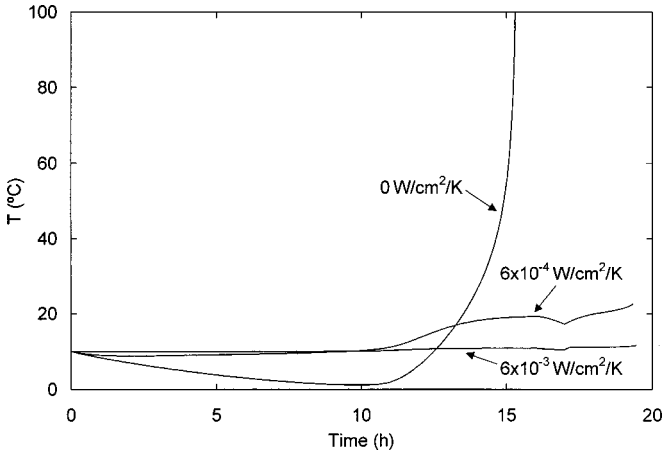

Figure 34. The model-predicted cell temperature at different heat transfer conditions at 10°C ambient temperature.

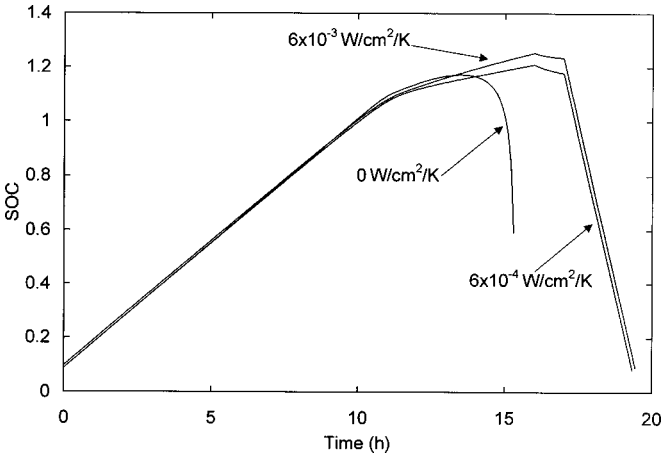

Figure 36. The model-predicted cell SOC at different heat transfer conditions at 10°C ambient temperature.

temperature reaches 100°C during the overcharge period for the adiabatic process. This indicates cell failure, and thus, the simulation terminates at that time point. For the process with the medium heat transfer coefficient, there is significant potential rollover during the overcharge period, which is a commonly observed phenomenon for nickel-hydrogen cells. Since the cell potential does not show rollover with a very high heat transfer rate, the cause of that phenomenon is attributed to the significant cell temperature rise during overcharge with the medium heat transfer rate, *i.e.*, the significant cell temperature rise during overcharge increases reaction rates and thus, less overpotentials are needed to maintain the same charge current. In Fig. 35, the cell pressure curves show little difference in three cases at the early period of the charge process. However, the adiabatic curve terminates the earliest. As shown in Fig. 36, the cell SOC differs significantly in three cases during the overcharge period. The cell SOC for the adiabatic process rapidly decreases with the sharp rise of the cell temperature. For the process with medium heat transfer coefficient, the slow cell SOC increase during the overcharge period is mainly caused by the significant rise of cell temperature.

Conclusions

Nickel phase reactions, including two parallel redox paths with different electron transfer numbers: β-$Ni(OH)_2$/β-NiOOH with 1.0 electron transfer and α-$Ni(OH)_2$/γ-NiOOH with 1.67 electron transfer, and two connecting reactions between them: α-$Ni(OH)_2$/β-$Ni(OH)_2$ and β-NiOOH/γ-NiOOH conversions, have been included in a nickel-hydrogen cell model, together with other important mechanisms. Comparison of model predictions with experimental data showed satisfactory results. From the model predictions, it is shown that nickel phase reactions have significant influence on the behavior of a nickel-hydrogen cell. The cell capacity variation at different temperatures, the change of KOH concentration between charge and discharge processes, and the cell potential rollover during the overcharge period, were satisfactorily explained with the model.

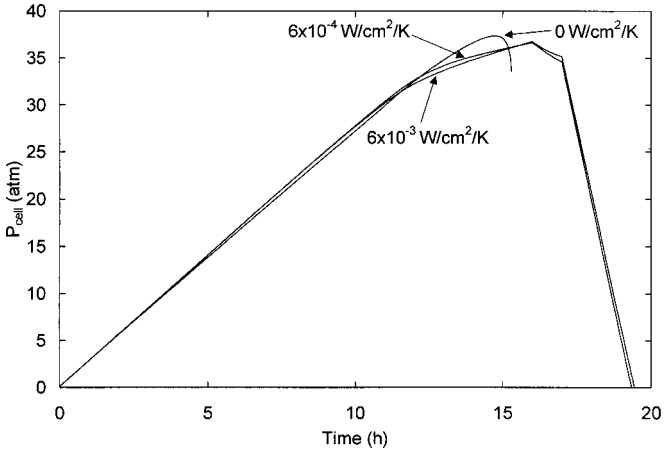

Figure 35. The model-predicted cell pressure at different heat transfer conditions at 10°C ambient temperature.

Acknowledgments

The authors wish to acknowledge the financial support provided by the Office of Research and Development of the United States Central Intelligence Agency.

The University of South Carolina assisted in meeting the publication costs of this article.

Appendix

Auxiliary model equations.—The current density on a unit area of the cell module

$$i_{app} = \frac{i_{cell}}{N_{module}\pi(r_{out}^2 - r_{in}^2)} \quad [A\text{-}1]$$

The maximum concentration of nickel active species

$$c_{H^+,max} = \frac{\rho_{Ni(OH)_2}}{M_{Ni(OH)_2}} \quad [A\text{-}2]$$

The porosity of the nickel electrode

$$\varepsilon_{pos} = \varepsilon_{0,pos} - \frac{L_{Ni(OH)_2}}{\rho_{Ni(OH)_2}}\varepsilon_{0,pos} \quad [A\text{-}3]$$

The radius of the nickel substrate in cylindrical shape

$$y_0 = \frac{2(1 - \varepsilon_{0,pos})}{a_0} \quad [A\text{-}4]$$

The radius of the nickel substrate covered with the nickel active material in cylindrical shape

$$y_1 = y_0\sqrt{1 + \frac{2(\varepsilon_{0,pos} - \varepsilon_{pos})}{y_0 a_0}} \quad [A\text{-}5]$$

The effective thickness of the nickel active material

$$l_y = \frac{(y_1^2 - y_0^2)}{2y_1} \quad \text{[A-6]}$$

The specific surface area of the nickel electrode

$$a_{pos} = a_0 \sqrt{\frac{1 - \varepsilon_{pos}}{1 - \varepsilon_{0,pos}}} \quad \text{[A-7]}$$

The molar concentration of the KOH electrolyte changes with temperature. It can be calculated based on the weight percent KOH concentration

$$c_e = \frac{W\rho_e}{5.61} \quad \text{[A-8]}$$

where the density of KOH electrolyte is given by

$$\rho_e = 1.09634853 - 4.217 \times 10^{-4}T + 1.173604 \times 10^{-2}W - 4.09 \times 10^{-6}TW \quad \text{[A-9]}$$

The conductivity of the KOH electrolyte

$$\kappa_e = -3.42000614 \times 10^{-3}T + 1.19699771 \times 10^{-5}T^2 - 1.17298091c_e - 5.16794041 \times 10^{-3}c_e^2 + 3.28292638 \times 10^{-3}Tc_e + 1.19604837 \times 10^2 c_e/T + 6.24311676 \times 10^{-4}c_e^3 - 1.88320099 \times 10^{-7}T^2c_e^2 \quad \text{[A-10]}$$

The diffusion coefficient of the KOH electrolyte

$$D_e = \exp(-16.489 + 0.02015T - 8.1607c_e^{0.5} + 286.2c_e - 2539.8c_e^{1.5} + 7207.5c_e^2) \quad \text{[A-11]}$$

The ratio of electrolyte concentration to water concentration

$$\frac{c_e}{c_0} = -1.4041 \times 10^{-4} + 18.2c_e + 100.25c_e^2 + 23811c_e^3 \quad \text{[A-12]}$$

The mean molar activity coefficient of the KOH electrolyte

$$f_{\pm} = \frac{1}{(-56c_e + 1.0002 + 45.726c_e - 601.63c_e^2)} \times \exp\left[\begin{array}{l} 10^3 \times c_e(0.06629 + 6.135 \times 10^{-4}T - 1.1018 \times 10^{-5}T^2 \\ + 4.096 \times 10^{-8}T^3)/(-56c_e + 1.0002 + 45.726c_e \\ - 601.63c_e^2) + 10^6 \times c_e^2(0.010909 - 1.7108 \times 10^{-4}T \\ + 1.6895 \times 10^{-6}T^2 - 7.969 \times 10^{-9}T^3)/(-56c_e \\ + 1.0002 + 45.726c_e - 601.63c_e^2)^2 + 10^9 \times c_e^3(-7.351 \times 10^{-4} \\ + 9.973 \times 10^{-6}T - 9.347 \times 10^{-8}T^2 + 6.215 \times 10^{-10}T^3/ \\ (-56c_e + 1.0002 + 45.726c_e - 601.63c_e^2)^3 + 10^{12} \\ \times c_e^4(1.5502 \times 10^{-5} - 1.98 \times 10^{-7}T + 1.8424 \times 10^{-9}T^2 \\ - 1.764 \times 10^{-11}T^3/(-56c_e + 1.0002 + 45.726c_e - 601.63c_e^2)^4 \\ + 31.6228 \times c_e^{0.5}(0.48742 + 5.4567 \times 10^{-4}T + 7.9888 \times 10^{-6}T^2) \\ /[1 + 44.7214 \times c_e^{0.5}/(-56c_e + 1.0002 + 45.726c_e - 601.63c_e^2)] \end{array}\right] \quad \text{[A-13]}$$

The constants in Henry's law for hydrogen and oxygen

$$K_{H_2} = \frac{1 - x_{H_2}}{RT(2c_e + 1.0 \times 10^{-7})x_{H_2}} \quad \text{[A-14]}$$

$$x_{H_2} = \frac{\exp\left[-48.1611 + \frac{5528.45}{T} + 16.8893\ln(0.01T)\right]}{10^{129c_e}} \quad \text{[A-15]}$$

$$K_{O_2} = \frac{1 - x_{O_2}}{RT(2c_e + 1.0 \times 10^{-7})x_{O_2}} \quad \text{[A-16]}$$

$$x_{O_2} = \frac{\exp\left(4.1741 - \frac{1.3104}{T} + \frac{3.417}{T^2} - \frac{2.4749}{T^3}\right)}{10^{[c_e(192.3 - 0.17T)]}} \quad \text{[A-17]}$$

The temperature difference in the cell stack

$$\Delta T_{stack} = T_{stack}|_{r=r_{in}} - T_{stack}|_{r=r_{out}} \quad \text{[A-18]}$$

List of Symbols

a_0	specific surface area of the nickel plaque, cm^2/cm^3
a_{pos}	specific surface area of the nickel electrode, cm^2/cm^3
a_{neg}	specific surface area of the platinum electrode, cm^2/cm^3
A_{vessel}	outside surface area of the cell pressure vessel, cm^2
C	rated capacity of the nickel-hydrogen cell, Ah
c_0	concentration of water solvent, mol/cm^3
c_e	concentration of the KOH electrolyte, mol/cm^3
$c_{e,ref}$	reference concentration of the KOH electrolyte, mol/cm^3
c_i	concentration of species i (i = β_-, β_+, α, γ), mol/cm^3
$c_{H^+,max}$	maximum concentration of nickel active species, mol/cm^3
$c_{i,ref}$	reference concentration of species i (i = β_-, β_+, α, γ), mol/cm^3
$c^g_{H_2}$	concentration of hydrogen in the gas phase, mol/cm^3
$c^g_{O_2}$	concentration of oxygen in the gas phase, mol/cm^3
c_{H_2}	concentration of hydrogen in the liquid phase, mol/cm^3
c_{O_2}	concentration of oxygen in the liquid phase, mol/cm^3
$c_{H_2,ref}$	reference concentration of hydrogen in the liquid phase, mol/cm^3
$c_{O_2,ref}$	reference concentration of oxygen in the liquid phase, mol/cm^3
$c_{p,cell}$	heat capacity of the nickel-hydrogen cell, J/K g
D_e	diffusion coefficient of the KOH electrolyte, cm^2/s
$\frac{dU^\theta_k}{dT}$	temperature coefficient of the equilibrium potential of reaction k, V
F	Faraday's constant, 96,487 C/eq
$f_{\pm}$	mean molar activity coefficient of the KOH electrolyte
h_{cell}	heat transfer coefficient between the cell and its surroundings, W/cm^2 K
h_{stack}	heat transfer coefficient between the cell stack and its surroundings, W/cm^2 K
i_{app}	applied current density on a unit area of the cell module, A/cm^2
i_{cell}	applied current on the nickel-hydrogen cell, A
i_l	current density in the liquid phase, A/cm^2
$i_{o,k,ref,T}$	exchange current density of reaction k at temperature T and reference reactant concentrations, A/cm^2
j_k	current density due to reaction k, A/cm^2
$i_{k,ref,T}$	rate of chemical reaction k at temperture T and reference reactant concentrations, A/cm^2
K_i	equilibrium constant relating the concentration of species i in the liquid to that in the gas phases
l_{neg}	thickness of the negative platinum electrode, cm
l_{pos}	thickness of the positive nickel electrode, cm
l_{sep}	thickness of the separator, cm
l_y	effective thickness of the nickel active material, cm
$L_{Ni(OH)_2}$	loading of active material in the porous nickel electrode, $g/(cm^3$ void volume)
m_{cell}	mass of the cell, g
$M_{Ni(OH)_2}$	molecular weight of $Ni(OH)_2$, g/mol
n_{H_2}	amount of hydrogen gas in the cell, mol
n_{O_2}	amount of oxygen gas in the cell, mol
N_{module}	number of cell modules in the nickel-hydrogen cell
P_{cell}	pressure of the cell, atm
p_{H_2}	partial pressure of hydrogen gas, atm
p_{O_2}	partial pressure of oxygen gas, atm
$p_{H_2,ref}$	reference pressure of hydrogen gas, atm
$p_{O_2,ref}$	reference pressure of oxygen gas, atm
$\dot{q}$	heat generation rate of a unit area of a cell module, $W/(s\ cm^2)$
r	radial coordinate of the cell stack, cm
r_{in}	electrode inner radius, cm
r_{out}	electrode outer radius, cm
R	universal gas constant, 8.3143 J/mol K
R_{cell}	internal electric resistance of metal leads and current collectors, Ω
t	time, s
t^*_-	transfer number of OH^-
T	cell temperature by assuming uniform temperature inside the cell, K
T_A	ambient temperature, K
T_{stack}	temperature in the cell stack, K
T_0	reference temperature, K
U^θ_k	standard equilibrium potential of reaction k, V
U^θ_{RE}	standard equilibrium potential of the Hg/HgO reference electrode, V
V_{cell}	potential of the nickel-hydrogen cell, V

V_{gas}	gas volume in the nickel-hydrogen cell, cm^3
W	weight percent concentration of the KOH electrolyte
x	*x* coordinate of the cell model, cm
x_{H_2}	mole fraction of hydrogen gas
x_{O_2}	mole fraction of hydrogen gas
y_0	radius of the nickel substrate in cylindrical shape, cm
y_1	radius of the nickel substrate covered with the nickel active material in cylindrical shape, cm

Greek

$\alpha_{a,k}$	anodic transfer number of reaction k
$\alpha_{c,k}$	cathodic transfer number of reaction k
$\Delta E_{a,k}$	activation energy of reaction k, J/mol
ΔU_k^{θ}	hysteresis OCP difference between charge and discharge processes for reaction k, V
$\varepsilon_{0,pos}$	porosity of the nickel plaque
ε_{pos}	porosity of the nickel electrode
$\varepsilon_{pos,l}$	porosity of the electrolyte in the nickel electrode
$\varepsilon_{sep,l}$	porosity of the electrolyte in the separator
ϕ_{pos}	potential of the current collector in the nickel electrode, V
ϕ_{neg}	potential of the current collector in the platinum electrode, V
ϕ_l	potential in the liquid phase, V
$\phi_{eq,k,T}$	equilibrium potential of reaction k at temperature T, V
$\phi_{eq,k,ref,T}$	equilibrium potential of reaction k at reference reactant concentrations and temperature T, V
λ_{stack}	thermal conductivity of the cell stack, W/cm K
η_k	overpotential of reaction k, V
κ_e	conductivity of the KOH electrolyte, S/cm
π	mathematical constant, 3.14159
ρ_e	density of the KOH electrolyte, g/cm^3
ρ_{stack}	density of the cell stack, g/cm^3
$\rho_{Ni(OH)_2}$	density of $Ni(OH)_2$, g/cm^3

References

1. J. D. Dunlop, G. M. Rao, and T. Y. Yi, *NASA Handbook for Nickel-Hydrogen Batteries*, NASA reference publication 1314 (1993).
2. Z. Mao, P. De Vidts, R. E. White, and J. Newman, *J. Electrochem. Soc.*, **141**, 54 (1994).
3. P. De Vidts, J. Delgado, and R. E. White, *J. Electrochem. Soc.*, **143**, 3223 (1996).
4. J. Kim, T. V. Nguyen, and R. E. White, *J. Electrochem. Soc.*, **139**, 2781 (1992).
5. J. Kim, T. Nguyen, and R. E. White, *J. Electrochem. Soc.*, **141**, 333 (1994).
6. P. De Vidts, J. Delgado, B. Wu, D. See, K. Kosanovich, and R. E. White, *J. Electrochem. Soc.*, **145**, 3874 (1998).
7. P. Timmerman, B. V. Ratnakumar, and S. Di Stefano, in *Aqueous Batteries*, P. D. Bennett and S. Gross, Editors, PV 96-16, p. 130, The Electrochemical Society Proceedings Series, Pennington, NJ (1996).
8. B. Paxton and J. Newman, *J. Electrochem. Soc.*, **144**, 3818 (1997).
9. S. Motupally, C. C. Streinz, and J. W. Weidner, *J. Electrochem. Soc.*, **145**, 29 (1998).
10. H. Bode, K. Dehmelt, and J. Witte, *Electrochim. Acta*, **11**, 1079 (1966).
11. P. C. Milner and U. B. Thomas, in *Advances in Electrochemistry and Electrochemical Engineering*, C. W. Tobias, Editor, Vol. 5, p. 1, Interscience, New York (1967).
12. J. McBreen, in *Modern Aspects of Electrochemistry*, R. E. White, J. O'M. Bockris, and B. E. Conway, Editors, No. 21, p. 29, Plenum Press, New York (1990).
13. A. Delahaye-Vidal, F. Portemer, B. Beaudoin, K. Tekaia-Elhsissen, P. Genin, and M. Figlarz, in *Nickel Hydroxide Electrodes*, D. A. Corrigan and A. H. Zimmerman, Editors, PV 90-4, p. 44, The Electrochemical Society Proceedings Series, Pennington, NJ (1989).
14. P. Oliva, J. Leonardi, J. F. Laurent, C. Delmas, J. J. Braconnier, M. Figlarz, F. Fievet, and A. de Guibert, *J. Power Sources*, **8**, 229 (1982).
15. R. Barnard, C. F. Randell, and F. L. Tye, in *Proceedings of the 12th International Symposium on Power Sources*, Brighton, U.K. (1981).
16. R. Barnard, C. F. Randell, and F. L. Tye, *J. Appl. Electrochem.*, **11**, 517 (1981).
17. R. Barnard, C. F. Randell, and F. L. Tye, *J. Appl. Electrochem.*, **13**, 97 (1983).
18. D. A. Corrigan and S. L. Knight, *J. Electrochem. Soc.*, **136**, 613 (1989).
19. S. G. Gratsch, *J. Phys. Chem. Ref. Data*, **18**, 1 (1989).
20. C. Lurie, B. Tobias, and P. Loeff, TRW Space and Electronics Group, Personal communication.